Sun-E: Dataset and Benchmark for Event-Based Sun Sensing

Sydney Dolan
Technical University of Munich
Lise-Meitner-Straße 9, 85521 Ottobrunn
sydney.dolan@tum.de

Alessandro Golkar
Technical University of Munich
Lise-Meitner-Straße 9, 85521 Ottobrunn
golkar@tum.de

Abstract

Event cameras are increasingly being explored for space applications due to their high dynamic range and increased spatiotemporal resolution. Existing datasets in this application have focused on capturing low-light, sub-pixel space objects and Earth observation scenarios. There remains a notable gap in datasets tailored to high-illumination conditions, particularly those involving direct solar imaging. This work introduces a dataset of solar event recordings captured with an event camera in a controlled sun-simulator environment. The dataset is specifically designed to support research in sun sensing and stray light analysis for spacecraft attitude estimation applications. It includes raw event data, annotated sun centroid locations, object motion profiles, and secondary optical aberration artifacts. In addition to the dataset, we present a systematic methodology for estimating the sun vector, intended to serve as a benchmark for evaluating sun sensing approaches in this application. All data and code are open source to facilitate further study: (`https://github.com/sydneyid/SunE`).

1. Introduction

Attitude sensors determine a spacecraft's orientation by sensing astronomical objects. Among attitude sensors, sun sensors are the most widely used due to their simplicity, low-power requirements, and the Sun's consistent visibility in space. Sun sensors estimate the direction and position of the sun relative to the spacecraft. Their working principle is shown in Figure 1. As the angle of incoming sunlight varies, the position of the projected sunspot shifts on the focal plane. This displacement is used to estimate the Sun's direction based off a known geometry. Following the notation of [13], the sunspot centroid (x_p, y_p) is extracted and the resultant Sun latitude α and azimuth β are computed as

$$\alpha = \arctan\left(\frac{\sqrt{W^2 \cdot (x_p - x_c)^2 + L^2 \cdot (y_p - y_c)^2}}{F}\right) \tag{1}$$

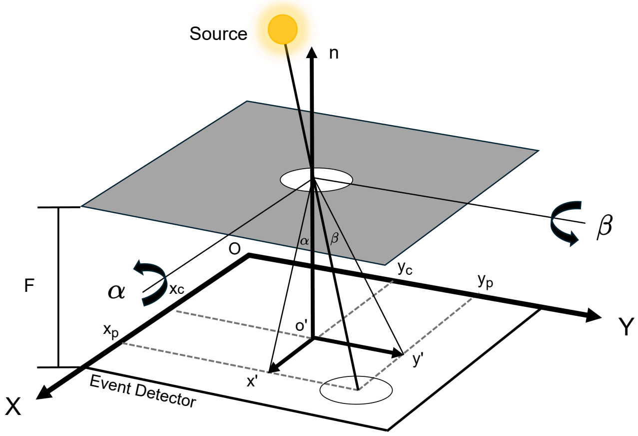

Figure 1. Ideal single-aperture sensor operating principle. The two sun angles α and β represent the relative sun angle. Figure adapted from [13].

$$\beta = \arctan\left(\frac{L \cdot (y_p - y_c)}{W \cdot (x_p - x_c)}\right) \tag{2}$$

where W and L are the length of a single pixel, (x_c, y_c) is the centroid of the region of interest when $\alpha = 0$, and F is the focal distance.

The performance of centroiding methods for sun sensing has plateaued due to limitations in spatial resolution, optical blur, and susceptibility to noise [5]. These constraints limit the achievable accuracy of sun sensors with conventional CMOS detectors. To address these challenges, we propose the use of event-based cameras for sun sensing.

Event cameras have a high dynamic range, which allows them to detect extremely bright and extremely dim objects. This makes them particularly well-suited for space environments, which often exhibit extreme lighting contrasts. This increased dynamic range can be attributed to the asynchronous functioning of event cameras. Each pixel in an event camera functions independently and generates an event when the logarithmic brightness intensity change exceeds a predefined threshold. An event is defined as

$e = [x, y, t, p]$., where (x, y) is the pixel coordinates, t represents the timestamp, and $p \in [0, 1]$ is the polarity of the change (where $p = 1$ is an increase in brightness and 0 is a decrease).

We adopt a maskless camera model where the sunspot centroid location (x_p, y_p) is identified via event-based centroiding techniques. The sun's direction is recovered through backprojection via known camera intrinsics K.

$$\mathbf{v}_{\text{sun}}^{\text{sensor}} = \frac{K^{-1} \cdot [x_p, y_p, 1]^T}{|K^{-1} \cdot [x_p, y_p, 1]^T|} \tag{3}$$

Traditional sun sensing often assume a masked configuration, where angular measurements are tightly coupled to the physical geometry of the sensor's aperture and detector layout. While those models are more dependent on the specific detector design (e.g., aperture mask, shape), the formulation presented here is primarily governed by the camera's intrinsic parameters, making it more generalizable across different imaging configurations. Under appropriate mappings between physical parameters and intrinsic calibration, both approaches are mathematically equivalent.

Despite the growing interest in event-based vision for space applications, there exists a notable lack of publicly available datasets specifically tailored for sun sensing. To date, no dedicated datasets, whether frame-based or event-based, exist for this application. This is a significant challenge to the development and evaluation of sun-sensing algorithms. Existing event camera datasets for space applications [3] feature objects that have more distinctive spatial characteristics and cannot be considered extensible to this application. Furthermore, while event-based versions of frame-based datasets have been introduced ([14]), these are commonly generated by applying noise models to synthetic event streams. As illustrated by a toy example in Figure 2, synthetic data diverges significantly from experimentally captured data. Synthetic event generators do not accurately model stray light artifacts within the scene. The underlying v2e ([14]) formulation does not account for optical interactions between the detector and lens or possible off-axis light effects impacting the detector. For cases like sun sensing, which involves observing high-intensity light illumination, accounting for stray light effects is important to realistically simulate sensor behavior.

The Sun emits high-intensity, broadband radiation, which can induce stray light interactions within the sun sensor. Incident light from the Sun can scatter off internal surfaces, causing optical artifacts like ghosts, scattered light, diffuse reflection, and edge diffraction. The impact of stray light is well known in optical system design and often requires expensive simulation and testing infrastructure to predict and address. Mitigation strategies often involve a combination of optical design and algorithmic processing techniques. Given the influence of stray light on optical performance and the high likelihood of such artifacts in sun sensor operation, realistic modeling of stray light effects is important to the development of a realistic sun-sensing dataset.

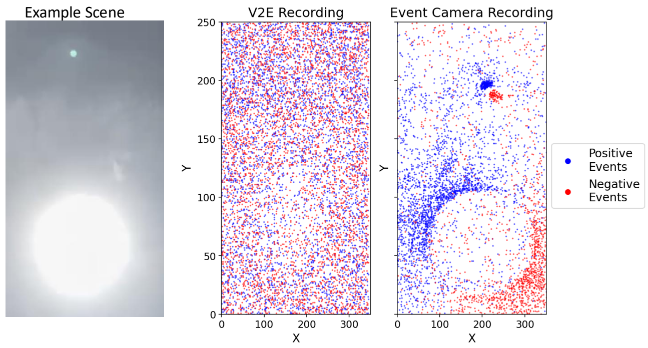

Figure 2. Example Comparison between simulated event-based solar imagery generated using v2e [14] and experimentally captured event-based data. The initial scene was captured outdoors and not in the laboratory set-up used to produce the Sun-E dataset. The cluster of events near the top of the Event Camera recording corresponds to a ghost optical artifact.

In this work, we address the broader gap in sun-sensing datasets by developing an experimental, high-fidelity dataset that captures realistic sunlight illumination and complex optical interactions. To this end, we introduce Sun-E, a novel dataset specifically designed for event-based sun sensing. The dataset consists of 9 scenes recorded with a fourth-generation event camera under varied sun angles, direction, and event sensor conditions. Each scene contains ground-truth metadata and auxiliary labels related to stray light analysis. In addition to the dataset, we provide a baseline methodology and evaluation protocol for event-based sun sensing. We summarize the key contributions of this paper as follows:

- We present an experimental dataset of nine labeled scenes under varying conditions of orientation, motion direction, and bias parameters. Each scene is designed to highlight challenges related to sun sensing and stray light analysis for this application, providing a controlled yet diverse benchmark.
- To support benchmarking and promote further research in event-based sun sensing, we implement a previously established sun sensing benchmark and introduce a new benchmark of our own. Both benchmarks, along with their evaluation tools, are open-sourced to enable reproducibility and community contribution.

The dataset and associated benchmark are released openly to support the development of event-based sun sensing algorithms. An overview of Sun-E , along with links to the code and the dataset, is available on our project page.

2. Related Work

2.1. Event Cameras for Space Situational Awareness and Astronomy

Event cameras have gained traction in space situational awareness (SSA) applications due to their high dynamic range. Early work by Cohen *et al.* [8] demonstrated the feasibility of event cameras for space applications. Using an event camera in conjunction with a ground telescope, they showed that event cameras can track both Low-Earth orbit and geosynchronous equatorial orbit objects during daytime. To improve the tracking reliability of this ground-based event camera system, Ralph *et al.* [18] proposed a slow-adapting network with an unsupervised feature extraction adaptive thresholds module [2] to learn spatiotemporal features and identify dim, sub-pixel objects. Arja *et al.* [3] proposed a contrast maximization framework for generating motion-compensated maps for Earth observation event data to improve feature visibility of event Earth observation data. McHarg *et al.* deployed an event camera onboard the International Space Station (ISS) and demonstrated event-based lightning detection in orbit after applying motion compensation to the event data [16].

Event cameras have also been applied to astronomical imaging. One of the earliest demonstrations was the capture of a total lunar eclipse by the International Centre for Neuromorphic Systems [15], although no official dataset or publication was produced. More recently, Cladera *et al.* [7] presented a stabilized recording of the 2024 total solar eclipse. Their work introduced a motion compensation algorithm specifically tuned for eclipse dynamics. Unlike direct sun observations, solar eclipses involve the light being blocked by the moon, preventing the full sun intensity from being detected.

2.2. Event Sun Sensors

In [10], the authors proposed a sun sensor with two event pixel rows in an L-shape. Sunlight angle was detected depending on which pixels were illuminated. Building on this initial concept, Gomez-Merchan *et al.* [12] introduced a temporal firing sensor (TFS) architecture that processes image data as a sequence of time-stamped events using a 64×64 pixel array. Within the TFS framework, a weighted centroid is computed across active pixels to estimate the sun vector, followed by a system reset. These models are limited by their reliance on custom-built sensors with a small number of pixels, achieving a reported accuracy of $2.37°$ in elevation (α) and $5.82°$ in azimuth (β). Our approach leverages a high-resolution commercial-off-the-shelf sensor, which enables higher spatial accuracy but also extended functionality to more general-purpose tasks beyond sun-sensing.

2.3. Event-Based Centroiding

Centroiding determines the precise location of an object in an image. Most event-based centroiding methods assume that events follow a Gaussian distribution centered around the object's location, thereby estimating the centroid via the spatial mean of positive events [4], or of all events [6]. An alternative approach for extracting higher-level structural features, such as prominent edges, involves the use of Hough Transforms. Centroids can then be extracted from Hough identified global parameteric shapes. Hough Transforms have previously been applied to event processing [17, 21], but these primarily focused on line segment variants. Extending these techniques to circular Hough Transforms introduces significant complexity, due to the increased parameter space across the time dimension.

3. The Sun-E Dataset

The Sun-E Dataset provides an event-based dataset for sun sensing. The goal of the dataset is to enable the analysis of centroiding techniques and stray light analysis under controlled, high-intensity lighting conditions. Table 1 provides a high-level dataset description.

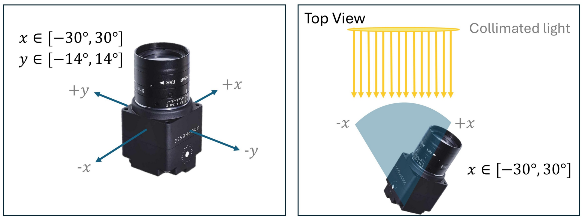

Figure 3. Left to Right: (a): Diagram of the sensor rig. All sensor axes are labeled. (b) Event camera collimating lens interaction.

All event sequences were recorded using a Sony-IMX 636 event sensor equipped with a 4 cm lens with an approximate field of view (FOV) of 8° horizontal and 10° vertical. The lens is attached to the sensor via C-mount interface, and the complete imaging system is fixed onto a two-axis motorized gimbal platform with gearbox backlash compensation. Figure 3 shows the motorized gimbal-axis configurations possible in this experimental setup. A fully calibrated variable-intensity sun simulator is used as a light source, capable of operating over a range of 0.1-1.1 solar constants. The simulator has been rated to Class B spatial non-uniformity of irradiance and Class A temporal instability specifications. The inclusion of the sun simulator represents a significant advancement over existing sun sensor work by enabling precise control and quantification of illumination levels, including the ability to replicate space-level solar intensities with high accuracy. In all dataset scene recordings, the sun intensity is controlled to be 1.0 solar constant. The surrounding environment outside of the sun

Alignment	ID	T	f#	Ghosts	Flares	Direction	MER	Biases
Center	1	60	5	✓	✓	Left	832.3	default
	2	20	5	×	✓	Down	649.6	default
	3	30	5	×	✓	Down	654.0	default
	4	58	8	✓	✓	Right	1224.7	default
Upper	5	58	5	×	✓	Right	750.4	default
	6	55	5	×	✓	Left	699.1	default
Lower	7	58	5	×	✓	Right	784.7	default
	8	58	5	×	✓	Left	782.1	default
	9	58	5	×	✓	Right	802.2	refractory

Table 1. Sequence description. T: total time in seconds, MER: Mean event rate (kiloevents/second).

simulator is covered with a shroud drape designed to mitigate any additional light sources.

A dedicated initialization routine defines the gimbal control trajectory by specifying the initial angle, angular velocity, and terminal angle with respect to the sun simulator. This script controls the angular path of the event sensor throughout each sequence. Using the defined initial and final angles, as well as the angular velocity, a time-stamped gimbal telemetry file is created to label the relative angle of the event camera to the sun simulator for each event sequence. All scenes in the dataset were generated with a controlled gimbal speed of $1^{\circ}/s$.

A corresponding event acquisition script interfaces with the event camera to initiate the recording, perform online hot pixel filtering, and save the resulting event stream data to HDF5 format. Hot pixel filtering is applied by default, as hot pixels are a known phenomenon in event cameras that cause individual pixels to fire erroneously high, leading to inflated file sizes and distortion of true event distribution. For each recording, the event camera biases are saved to preserve the contrast thresholds used for event generation. The script also saves the measured temperature reading, calibrated camera intrinsic matrix, and measured illumination levels reported by the camera drivers.

3.1. Annotations

For each sequence in the dataset, we provide the following annotations:

Sun Vector Analysis: Each sequence includes time-stamped solar geometry parameters derived from the programmed gimbal mount trajectory. These include the centroid of the sun spot in the image plane, as well as the corresponding solar latitude (α) and azimuth (β). This information is computed directly from the mounting script and gimbal control signals.

Optical Aberration Artifacts. Sequences exhibiting stray light artifacts, such as ghosts, are annotated. For each detected ghost artifact, we provide its image-plane centroid, estimated spatial extent (radius), and time of occurrence. These annotations were manually labeled and subsequently verified to ensure that the ghost motion exhibited temporal consistency with the overall motion observed in the sequence.

Event and Simulation Metadata. All event recordings have been preprocessed to remove spurious noise sources such as persistent hot pixels. Each sequence is stored in HDF5 format and includes metadata fields capturing key acquisition parameters, including event camera bias settings, solar intensity, event rate statistics, focal length, and the intrinsic calibration matrix (K).

3.2. Sequences

A comprehensive list of sequences along with summary statistics is provided in Table 1. The dataset contains three possible alignment configurations: center, lower, and upper. The alignment configuration refers to the approximate relative orientation of the event camera with respect to the sun simulator. Specifically, whether the sensor is aligned from face-on, from above, or from below. These alignments were used to induce varying stray light effects in the recorded event streams. Changes in the relative angles between the sun simulator and the event camera result in different light ray incidence angles, thereby producing distinct optical artifacts. For example, ghost artifacts were most prominent in the center alignment. We also evaluated a range of aperture settings (f/#) to assess their influence on observed phenomena. We observed minimal differences in observed phenomena at higher f/# values. In contrast, lower $f\#$'s led to immediate sensor saturation, rendering the data unusable. The f/# values in the dataset were selected because they produced a clear solar artifact while also exhibiting clear stray light interactions. Aperture configuration and lens design are important components of the broader optical system affecting stray light, but additional investigation into their selection and analysis falls outside the scope of this work.

Representative event frames from the dataset, along with the corresponding annotations, are shown in Figures 4-5. Figure 4 illustrates a sample event frame accumulated over a $10ms$ window, corresponding to Sequence ID 1, with sunspot centroid and ghost annotations overlaid. This frame

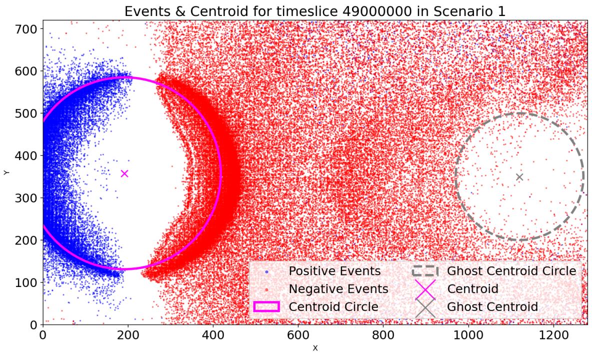

Figure 4. Scene ID 1 Event Frame, accumulation time 10 ms

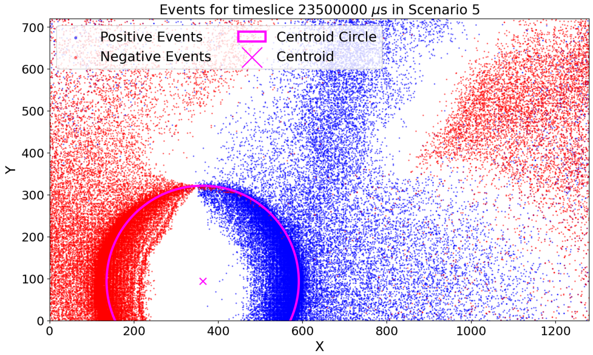

Figure 5. Scene ID 5 Event Frame, accumulation time 10 ms

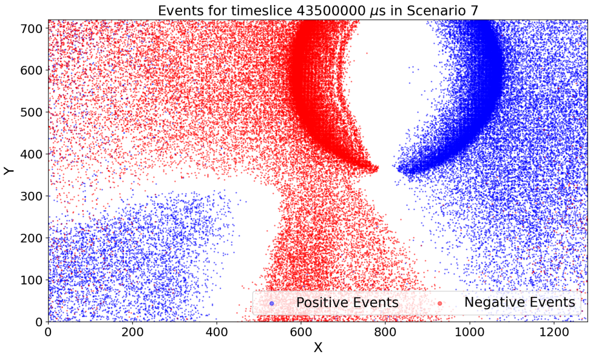

Figure 6. Scene ID 7 Event Frame, default bias settings

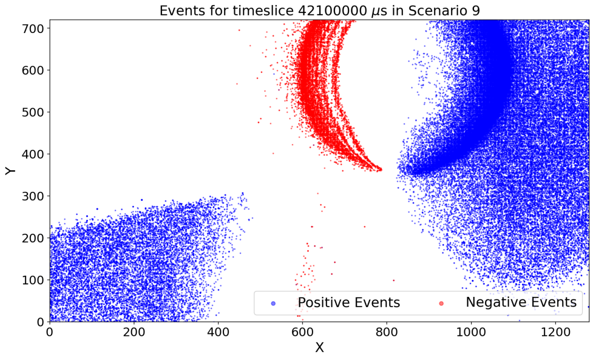

Figure 7. Scene ID 9 Event Frame, altered bias settings

exhibits several noteworthy phenomena that, to the best of our knowledge, have not been previously reported in the literature concerning event-based cameras. Most prominently, a ”black sun” artifact is observed. A ”black sun” is an area of sensor saturation where pixel activity ceases [20]. Due to the sensitivity of the event camera, noise events may be reported even in the absence of illumination. The region near the centroid exhibiting a low event count likely indicates a saturated area caused by the sun’s light intensity. This results in a lack of reported events relative to the average background event density. The event frame also reveals significant optical aberrations. Notably, on the right side of the frame, a secondary, faint circular pattern is present. These patterns, commonly referred to as ghosts [1], occur when a secondary light path is formed through an even number of internal reflections within the optical system, resulting in a duplicate, misaligned image. Such ghost artifacts are important considerations for software approaches aimed at mitigating stray light effects. Figure 5 illustrates an event frame from Scenario ID 5. Distinct regions of both positive and negative event activity indicate off-axis illumination effects. As the relative angle of the sun simulator changes over time, these regions shift accordingly, suggesting the formation of new off-axis, secondary regions within the sensor, as well as the fading of previously illuminated regions.

We also explored the impact of sensor bias selection when creating the dataset. Scenario ID 9 is one such example, and was recorded using an alternative bias setting that has a longer refractory period, meaning that there is a longer period of time during which a pixel is blind. This scenario can be used as a reference for assessing the generalizability of algorithms to different bias settings. Figures 6 and 7 compare Scenarios ID 7 and 9 under similar solar incidence angles. Although both event frames correspond to equivalent illumination geometry, Scenario 7 produces a significantly higher number of negative events. This more balanced event distribution leads to greater prominence of flare artifacts in Scenario 7 compared to Scenario 9.

While bias configuration selection significantly influenced the background activity noise, the overall event recording of the sun itself was not substantially impacted. We also posit that one of the values of this dataset lies in its inclusion of realistic and challenging stray light artifacts. The conditions posed in this dataset highlight examples where conventional algorithms that rely on strict alignment assumptions may fail or underperform. Consequently, detailed bias tuning and optimization are beyond the scope of this work and are left as directions for future research.

Sequence	1			2			3			4		
	D	$\|\|\alpha_{err}\|\|$	$\|\|\beta_{err}\|\|$	D	$\|\|\alpha_{err}\|\|$	$\|\|\beta_{err}\|\|$	D	$\|\|\alpha_{err}\|\|$	$\|\|\beta_{err}\|\|$	D	$\|\|\alpha_{err}\|\|$	$\|\|\beta_{err}\|\|$
TFS [9]	0.993	5.78	0.857	0.995	0.309	0.399	0.86	1.364	2.187	0.996	12.899	1.602
Sun-E (ours)	0.955	2.382	0.233	0.875	0.227	3.485	0.873	0.203	3.827	0.952	1.165	0.491

Table 2. Comparison across methods in the center alignment. D is the detection rate (higher is better), $||\alpha_{err}||$ is the normalized solar latitude error (lower is better), and $||\beta_{err}||$ is the normalized solar azimuth error (lower is better).

4. Benchmark

Our dataset enables the evaluation and comparison of existing algorithms designed for event-based sun sensing. Where applicable, we adapted existing sun-sensing algorithms to our maskless sensor configuration for direct comparison. We also propose a new sun-sensing method, developed in conjunction with this dataset, to serve as a baseline. Implementations of both methods are provided alongside the dataset.

We introduce several metrics for evaluation. The detection rate, D quantifies the proportion of successful detections over the sequence. Detections are synchronized with ground-truth gimbal azimuth and elevation measurements recorded at 0.1-second intervals, and the detection rate is computed accordingly. It is important to note that a detection rate does not necessarily indicate an accurate match, it is a metric used to indicate the convergence of the system results. $||\alpha_{err}||$ represents the mean normalized error between the estimated and true sun latitude, whereas $||\beta_{err}||$ represents the mean normalized error between estimated and true sun azimuth.

Benchmarked Methods. We briefly describe the other benchmark method, with additional supplementary information provided in the Appendix. *TFS* [9] applied a weighted centroid approach, where the centroid is determined by the most active events. We extend this formulation to accommodate maskless camera models, which feature a larger pixel array. Our approach first applies a weighted model to identify regions with the highest event activity, followed by a Hough transform applied within these regions to accurately determine the centroid. This use of the Hough transform compensates for the absence of inherent masked structural elements in maskless sensors, which otherwise aid in producing a distinct sunspot pixel signature. Due to the black sun effect, no events are reported at the sun's centroid, making this modified approach necessary since the weighted center of reported events does not align with the actual sunspot center.

Sun-E Proposed Benchmark Method We proposed our own sun-sensing centroiding estimation technique, *Sun-E*, informed by the phenomena observed in this dataset. Our technique to estimate centroid location is described in Algorithm 1. More details are provided in this section.

Algorithm 1: Sun-E Sun-Spot Tracking Method

```
Input: Time period $\mathbb{T}$, camera intrinsic matrix $K$,
  sun density threshold $\rho$
Separate events over interval $\mathbb{T}$ into $\mathcal{E}_{\mathbb{T}}^{+},\ \mathcal{E}_{\mathbb{T}}^{-}$
Compute event frame $\mathcal{F}_{\mathbb{T}}^{+}$ from $\mathcal{E}_{\mathbb{T}}^{+}$
Extract contour set $\{\mathcal{C}_j\}$ from $\mathcal{F}_{\mathbb{T}}^{+}$
Predict Kalman state:
  $\mathbf{x}_{k|k-1}, \mathbf{P}_{k|k-1} \leftarrow \text{KalmanPredict}(\mathbf{x}_{k-1}, \mathbf{P}_{k-1})$
Extract predicted centroid position:
  $\mathbf{c}_{pred} \leftarrow [x_{k|k-1}, y_{k|k-1}]^{\top}$
Define best candidate score $\mathcal{S}_{best} \leftarrow -\infty$
for each contour $\mathcal{C}_j$ do
    $(\mathrm{c}_j, r_j) = \arg\min_{\mathbf{c},r} \sum_i \left(\|\mathbf{p}_i - \mathbf{c}\|^2 - r^2\right)^2$
    Compute solar density score, $\rho_j$
    Compute central suppression score: $\rho_j^{\text{center}}$
    Compute arc density score: $\rho_j^{\text{arc}}$
    Kalman Consistency penalty: $p_j = \exp(-\gamma\delta_j^2)$;
    Score candidate as: $\mathcal{S}_j$
    if $\mathcal{S}_j > \mathcal{S}_{best}$ then
        $\mathcal{S}_{\text{best}} \leftarrow (\mathbf{c}_j, r_j)$
        $\hat{\mathbf{z}}_k \leftarrow \mathbf{c}_j$
    end
end
$(\mathbf{x}_k, \mathbf{P}_k) \leftarrow$
  $\begin{cases} \text{KalmanUpdate}(\mathbf{x}_{k|k-1}, \mathbf{P}_{k|k-1}, \hat{\mathbf{z}}_k), & \text{if } \hat{\mathbf{z}}_k \neq \varnothing \\ (\mathbf{x}_{k|k-1}, \mathbf{P}_{k|k-1}), & \text{otherwise} \end{cases}$
```

Let the event stream be defined as a set of events:

$$\mathcal{E} = \{e_i = (x_i, y_i, t_i, p_i) \mid i = 1, 2, ..., N\} \tag{4}$$

where (x_i, y_i) is the pixel coordinate, t_i is the timestamp, and $p_i \in \{+1, -1\}$ indicates the event polarity (positive or negative). We define a time frame $\mathbb{T}$ to collect a 3D point set of the event recording. This point set is split into positive and negative polarities.

$$\mathcal{E}_{\mathbb{T}}^{\pm} = \{(x_i, y_i, t_i) \,|\, t_i \in \mathbb{T},\ p_i = \pm 1\} \tag{5}$$

Positive polarity events are used for initial contour extraction from the event cloud, due to their higher temporal precision and stronger correlation with the true boundary of the incident light source, as previously demonstrated

Sequence	**5**			**6**			**7**			**8**			**9**		
	D	$\|\|\alpha_{err}\|\|$	$\|\|\beta_{err}\|\|$	D	$\|\|\alpha_{err}\|\|$	$\|\|\beta_{err}\|\|$	D	$\|\|\alpha_{err}\|\|$	$\|\|\beta_{err}\|\|$	D	$\|\|\alpha_{err}\|\|$	$\|\|\beta_{err}\|\|$	D	$\|\|\alpha_{err}\|\|$	$\|\|\beta_{err}\|\|$
TFS [9]	0.964	7.677	2.862	0.962	7.870	2.301	0.986	6.553	2.434	0.926	5.597	2.204	0.234	7.232	3.8325
Sun-E (ours)	0.958	2.713	0.4921	0.992	1.579	0.376	0.965	4.323	1.454	0.967	2.831	0.335	0.939	5.064	0.915

Table 3. Comparison across Sequences 5–9 for each method. D is the detection rate (higher is better), $||\alpha_{err}||$ is the normalized solar latitude error (lower is better), and $||\beta_{err}||$ is the normalized solar azimuth error (lower is better).

in [4,19]. A binary event frame is generated using only positive events, and a standard contour detection algorithm [22] is applied to extract prominent contours. Each identified contour is then approximated by fitting a circle using a least squares initialization.

Candidate circles are evaluated on two primary criteria. First, the solar density score ρ is computed within the candidate circular region, based on the combined number of positive and negative events.

$$\rho_j = \frac{1}{|\mathcal{E}_k|} \sum_{e_i \in \mathcal{E}_k} \left(\sqrt{(x_i - x_j)^2 + (y_i - y_j)^2} \leq r_j \right) \tag{6}$$

A smaller sub-region centered at the circles centroid is also examined. This region is expected to be saturated and thus contain few or no events, thus providing a negative correlation cue.

$$\rho_j^{\text{center}} = \sum_{e_i \in \mathcal{E}_k} \left(\sqrt{(x_i - x_j)^2 + (y_i - y_j)^2} \leq \epsilon r_j \right) \tag{7}$$

Second, an arc density metric is applied, which measures the concentration of events along the fitted arc. Viable circle candidates are expected to exhibit a high arc density.

$$\rho_j^{\text{arc}} = \sum_{e_i \in \mathcal{E}_k} \left(\left| \sqrt{(x_i - x_j)^2 + (y_i - y_j)^2} - r_j \right| \leq \delta \right) \tag{8}$$

A Kalman filter is integrated to enforce temporal consistency in centroid tracking. At each time interval $\mathcal{T}$, the filter predicts the state vector $x_{k|k-1}$, which has the centroid position and velocity. The consistency is quantified via a penalty term p_j, where δ_j represents the Euclidean distance between the candidate centroid and the predicted state, and γ controls the penalty strength. This makes the final score computation used to identify candidate circles.

$$\mathcal{S}_j = \left(\rho_j^{\text{arc}} - \lambda \cdot \rho_j^{\text{center}} \right) \cdot p_j \tag{9}$$

Candidates that deviate significantly from the predicted centroid receive lower scores. The candidate with the highest combined score is used as the observation $\hat{z}_k$ to update the Kalman filter state via the standard measurement update step, thus refining future predictions. If no candidate passes the consistency check, the filter state is propagated without correction, maintaining a smooth trajectory over time.

Performance in Center Aligned Scenes Table 2 shows the results of the associated benchmarks for dataset Scene IDs 1-4. For Sun-E, the average $||\alpha_{err}||$ across scenes was 0.994 and average $||\beta_{err}||$ was 2.009. In comparison, fine sun sensors typically require angular accuracies below 1°, while coarse sun sensors operate within a 1–5°range. These results place Sun-E at the upper bound of fine sun sensor performance. However, further refinement is needed in the processing pipeline to consistently achieve the sub-degree accuracy required for reliable fine sun sensing, and significantly more to approach star tracker-level precision (i.e., 0.01–0.1°).

Sun-E exhibits the highest $||\beta_{err}||$ error across all scenes on scenes 2 and 3, despite the sun remaining fully in frame throughout these sequences. This suggests a potential limitation in the method's ability to track vertical motion consistently. Additionally, these shorter-duration scenes ($T < 30$ seconds) may provide insufficient temporal data for the Kalman filter to effectively converge and correct fitting errors. In contrast, longer sequences appear to improve filter stability and overall orientation accuracy.

TFS was most accurate on the downward vertical motion scenes (ID's 2 and 3). The lateral movement scenes exhibited higher error; this in part can be attributed to the fact that a larger portion of the sun completely exits the frame. TFS achieved an average $||\alpha_{err}||$ of 5.088 and average $||\beta_{err}||$ of 1.681. This is comparable to the results from the original L-slit method, indicating that our adaptation preserves its core performance characteristics. In Scene 4, the TFS $||\alpha_{err}||$ was significantly larger than in other scenes. This scene has a slightly larger $(f\#)$ resulting in a smaller apparent sunspot radius. This scene has a thicker characteristic arc width, leading to a higher mean event rate than observed in other scenes, which also increases the overall edge ambiguity. This scene also includes prominent ghost artifacts, which produce circular, sunspot-like shapes in frame (see Fig. 8 for an example). The additional features introduced ambiguity in the detection process as Hough transform methods are sensitive to noise.

The performance of this technique is highly dependent on the sun's position and visibility within the frame; accurate results are more likely when the sun is fully visible and unobstructed. However, the absence of frame-to-frame tracking limits the system's ability to reject implausible or inconsistent estimates.

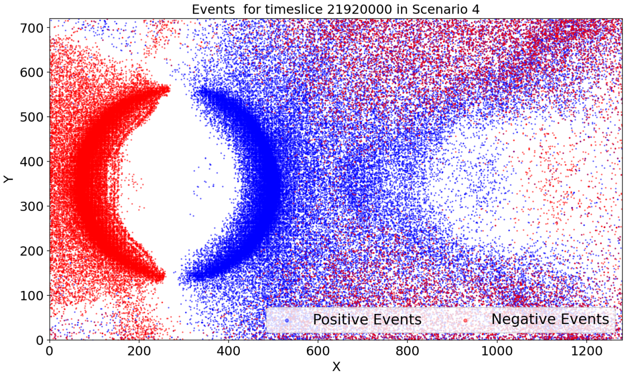

Figure 8. Scene ID 4, Event Frame, $f\# = 8$

Performance in Off-Center Aligned Scenes Table 3 shows the results of the associated benchmarks for dataset Scene IDs 5-9. In these off-center alignments, Sun-E produces more accurate $||\beta_{err}||$ estimates, with $||\alpha_{err}||$ producing roughly comparable rates to its performance on Scene IDS 1-4. The average $||\alpha_{err}||$ across scenes was 3.302 and average $||\beta_{err}||$ was 0.714. This is likely due to the arc fitting approach, which is better suited to partially occluded depictions of the sun. By contrast, TFS performs poorly both in orientation estimations under these conditions. It has an average $||\alpha_{err}||$ of 6.983 and average $||\beta_{err}||$ of 2.727. Partial sun visibility likely disrupts the symmetry required for accurate Hough-based fitting. These results suggest that Sun-E is less sensitive to scene-dependent factors such as alignment and bias settings, whereas TFS performance is strongly dependent on idealized viewing conditions.

5. Conclusion

We present Sun-E, a user-friendly annotated event dataset, and several benchmarks. Our presented dataset enables the analysis of event camera performance in high-intensity illumination conditions. Sun-E includes challenging scenarios such as partial sun-visibility, optical artifacts, and dynamic motion. We include additional annotations to support the usage and interaction with this dataset, like the relative sun angle, bias parameters, ghost labeling, and illumination levels.

We implement an existing event-based sun sensing technique and introduce our own sun sensing technique as a benchmark for this application. Our benchmark currently achieves coarse sun sensor level accuracy, with further advancements required to meet fine sun sensor level precision. We release Sun-E publicly to support the development and evaluation of future event-based sun sensing algorithms, and to encourage future research on stray light modeling in event-based systems.

Limitations. During dataset recording, the two-axis rotation table used for the gearbox rotation caused minor vibrations. This led to occasional discontinuities in the captured event stream. We note that the resulting breaks in continuity are subtle but may be of interest to researchers relying on the temporal consistency of the event data. Finally, the dataset is not general purpose. It is explicitly designed for sun sensing applications and does not include scenarios involving both a dominant sun-like illumination source and additional dynamic or static objects within the field of view. This would be an interesting area for future dataset development to explore the feasibility of event cameras in dual-purpose applications

Future Work. The presented work could be used for evaluating and performing additional tasks, such as:

- **Stray Light Artifact Filtering.** In the implemented benchmarks, only hot pixel removal was applied. Future work could focus on more precise mitigation of stray light effects, such as modeling the sun's motion to estimate potential ray paths responsible for ghost artifacts, and subsequently excluding or de-weighting affected regions. Alternatively, spatial or temporal filtering strategies could be developed to suppress these artifacts in the initial processing of the data.
- **Contrast Maximization:** Additional pre-processing techniques for event-based motion, such as contrast maximization [11], were not applied in this work. Integrating such methods could be a promising direction for future research, particularly in enhancing optical flow estimation and overall event-based motion analysis. In principle, contrast maximization could also improve arc sharpness and increase the accuracy of centroid estimation.
- **Object Tracking under High Illumination.** Because of the precise timestamped sunspot modeling of the sunspot centroid, this data set can be used for event-based object tracking. As this data focuses on high intensity light, it can be used to study how well methods developed for low-light scenarios (e.g. such as star tracking [19]) generalize.
- **Synthetic Event Data Generations.** As demonstrated in Figure 2, synthetic event generators do not model complex optical interaction. This dataset can be leveraged to develop empirical approximations for optical phenomena. This enables the use of the dataset as experimental ground truth for validating and refining event simulation models, ultimately supporting the development of more physically realistic event-based rendering pipelines.

6. Acknowledgments

Sydney Dolan is funded by the Federal Ministry for Economic Affairs and Climate Action (BMWK) through the German Aerospace Center (DLR) (Grant No. 50LZ2402). Thank you to Pierre Goux for his help and insight in collecting the recordings associated with the dataset.

References

[1] Rania Hassan Abd El-Maksoud. *Ghost image analysis for optical systems*. Phd thesis, The University of Arizona, 2009. 5

[2] Saeed Afshar, Nicholas Ralph, Ying Xu, Jonathan Tapson, André van Schaik, and Gregory Cohen. Event-based feature extraction using adaptive selection thresholds. *Sensors*, 20(6):1600, 2020. 3

[3] Sami Arja, Alexandre Marcireau, Richard L Balthazor, Matthew G McHarg, Saeed Afshar, and Gregory Cohen. Density invariant contrast maximization for neuromorphic earth observations. In *Proceedings of the IEEE/CVF Conference on Computer Vision and Pattern Recognition*, pages 3984–3994, 2023. 2, 3

[4] Samya Bagchi and Tat-Jun Chin. Event-based star tracking via multiresolution progressive hough transforms. In *Proceedings of the IEEE/CVF Winter Conference on Applications of Computer Vision*, pages 2143–2152, 2020. 3, 7

[5] Jingyu Bao, Haiyang Zhan, Ting Sun, Fei Xing, and Zheng You. Adaptive energy filtering method based on time-domain image sequences for high-accuracy spot target localization. *Applied Optics*, 61(11):3034–3047, 2022. 1

[6] Tat-Jun Chin, Samya Bagchi, Anders Eriksson, and Andre Van Schaik. Star tracking using an event camera. In *Proceedings of the IEEE/CVF Conference on Computer Vision and Pattern Recognition Workshops*, pages 0–0, 2019. 3

[7] Fernando Cladera, Kenneth Chaney, Caroline Pritchard, M. Ani Hsieh, Vijay Kumar, Camillo J. Taylor, and Kostas Daniilidis. Looking into the shadow: Recording a total solar eclipse with high-resolution event cameras. In *Proceedings of the IEEE/CVF Conference on Computer Vision and Pattern Recognition (CVPR) Workshops*, pages 4988–4992, June 2025. 3

[8] Gregory Cohen, Saeed Afshar, Brittany Morreale, Travis Bessell, Andrew Wabnitz, Mark Rutten, and André van Schaik. Event-based sensing for space situational awareness. *The Journal of the Astronautical Sciences*, 66(2):125–141, Jan. 2019. 3

[9] Lukasz Farian, Pablo Fernandez-Peramo, Philipp Hafliger, and Juan A Lenero-Bardallo. Centroid estimation method with sub-pixel resolution for event-based sun sensors. In *2022 17th Conference on Ph.D Research in Microelectronics and Electronics (PRIME)*. IEEE, June 2022. 6, 7

[10] Łukasz Farian, Philipp Häfliger, and Juan A. Leñero-Bardallo. Miniaturized sun sensor with in-pixel processing for attitude determination of micro space probes. In *2015 International Conference on Event-based Control, Communication, and Signal Processing (EBCCSP)*, pages 1–6, 2015. 3

[11] Guillermo Gallego, Henri Rebecq, and Davide Scaramuzza. A unifying contrast maximization framework for event cameras, with applications to motion, depth, and optical flow estimation. In *Proceedings of the IEEE conference on computer vision and pattern recognition*, pages 3867–3876, 2018. 8

[12] Ruben Gomez-Merchan, Juan Antonio Leñero-Bardallo, María López-Carmona, and Ángel Rodríguez-Vázquez. A low-latency, low-power cmos sun sensor for attitude calculation using photovoltaic regime and on-chip centroid computation. *IEEE Transactions on Instrumentation and Measurement*, 72:1–12, 2023. 3

[13] Michael Herman, Olivia J. Pinon Fischer, and Dimitri N. Mavris. Sun sensor calibration algorithms: A systematic mapping and survey, 2025. 1

[14] Yuhuang Hu, Shih-Chii Liu, and Tobi Delbruck. v2e: From video frames to realistic dvs events. In *Proceedings of the IEEE/CVF conference on computer vision and pattern recognition*, pages 1312–1321, 2021. 2

[15] International Centre for Neuromorphic Systems. Full Lunar Eclipse through a Neuromorphic Event-based Camera. `https://www.westernsydney.edu.au/icns/resources/research_videos/full_lunar_eclipse_through_a_neuromorphic_event-based_camera`, n.d. [Accessed: 2025-03-16]. 3

[16] Matthew G. McHarg, Richard L. Balthazor, Brian J. McReynolds, David H. Howe, Colin J. Maloney, Daniel O'Keefe, Rayomand Bam, Gabriel Wilson, Paras Karki, Alexandre Marcireau, and Gregory Cohen. Falcon neuro: an event-based sensor on the international space station. *Optical Engineering*, 61(08), Aug. 2022. 3

[17] Zhenjiang Ni, Aude Bolopion, Joël Agnus, Ryad Benosman, and Stéphane Regnier. Asynchronous event-based visual shape tracking for stable haptic feedback in microrobotics. *IEEE Transactions on Robotics*, 28(5):1081–1089, 2012. 3

[18] Nicholas Ralph, Damien Joubert, Andrew Jolley, Saeed Afshar, Nicholas Tothill, André Van Schaik, and Gregory Cohen. Real-time event-based unsupervised feature consolidation and tracking for space situational awareness. *Frontiers in neuroscience*, 16:821157, 2022. 3

[19] Albert W Reed, Connor Hashemi, Dennis Melamed, Nitesh Menon, Keigo Hirakawa, and Scott McCloskey. Ebs-ekf: Accurate and high frequency event-based star tracking. In *Proceedings of the Computer Vision and Pattern Recognition Conference*, pages 6510–6519, 2025. 7, 8

[20] Rashid Saleem and Sukhan Lee. Accurate and cost-effective micro sun sensor based on cmos black sun effect. *Sensors*, 19(3):739, Feb. 2019. 5

[21] Sajjad Seifozzakerini, Wei-Yun Yau, Bo Zhao, and Kezhi Mao. Event-based hough transform in a spiking neural network for multiple line detection and tracking using a dynamic vision sensor. In *BMVC*, volume 94, pages 1–12. York, UK, 2016. 3

[22] Satoshi Suzuki et al. Topological structural analysis of digitized binary images by border following. *Computer vision, graphics, and image processing*, 30(1):32–46, 1985. 7